

1 **Illuminating a Contorted Slab with a Complex Intraslab** 2 **Rupture Evolution during the 2021 M_W 7.3 East Cape, New** 3 **Zealand Earthquake**

4 **Ryo Okuwaki^{1,2,3,=}, Stephen P. Hicks^{4, =}, Timothy J. Craig³, Wenyan Fan⁵, Saskia**
5 **Goes⁴, Tim J. Wright³, and Yuji Yagi²**

6 ¹Mountain Science Center, University of Tsukuba, Tsukuba, Ibaraki 305-8572, Japan

7 ²Faculty of Life and Environmental Sciences, University of Tsukuba, Tsukuba, Ibaraki 305-8572, Japan

8 ³COMET, School of Earth and Environment, University of Leeds, Leeds LS2 9JT, UK

9 ⁴Department of Earth Science and Engineering, Imperial College London, London SW7 2AZ, UK

10 ⁵Scripps Institution of Oceanography, UC San Diego, La Jolla, California 92093, USA

11 **Key Points:**

- 12 • A moment magnitude 7.3 2021 East Cape, New Zealand intraslab earthquake
- 13 comprised multiple rupture episodes with different faulting styles
- 14 • The complex rupture comprises components of shallow trench-normal extension
- 15 and unexpectedly, deep trench-parallel compression in slab
- 16 • The trench-parallel compression likely reflects stress rotation at a buoyancy contrast
- 17 that drives slab contortion

⁼Equally contributing author

Corresponding author: Ryo Okuwaki, rokuwaki@geol.tsukuba.ac.jp

18 **Abstract**

19 The state-of-stress within subducting oceanic plates controls rupture processes of deep
20 intraslab earthquakes. However, little is known about how the large-scale plate ge-
21 ometry and the stress regime relate to the physical nature of the deep-intraslab earth-
22 quakes. Here we find, by using globally and locally observed seismic records, that the
23 moment magnitude 7.3 2021 East Cape, New Zealand earthquake was driven by a com-
24 bination of shallow trench-normal extension and unexpectedly, deep trench-parallel
25 compression. We find multiple rupture episodes comprising a mixture of reverse, strike-
26 slip, and normal faulting. Reverse faulting due to the trench-parallel compression is
27 unexpected given the apparent subduction direction, so we require a differential-buoyancy
28 driven stress rotation which contorts the slab near the edge of the Hikurangi plateau.
29 Our finding highlights that buoyant features in subducting plates may cause diverse
30 rupture behavior of intraslab earthquakes due to the resulting heterogeneous stress
31 state within slabs.

32 **Plain Language Summary**

33 A key type of tectonic boundary is where two plates collide with one sinking into the
34 mantle beneath. These subduction zones generate the world's largest earthquakes. Quan-
35 tifying stress in the subducting plate ("slab") is important because slabs drive the global
36 plate-tectonic system, and large earthquakes can occur within them. These earthquakes
37 can cause strong shaking, and, when occurring near cities, can lead to damage. How-
38 ever, mapping stress is challenging as we cannot directly "see" inside deep slabs. Our
39 best indications of slab stress come from earthquakes themselves. A magnitude 7.3
40 earthquake north of New Zealand in 2021 generated a distinct pattern of seismic wave-
41 forms at seismometers installed worldwide. We used these seismic records to probe
42 the earthquake, providing a new view of stress in subduction zones. We found the earth-
43 quake generated both vertical and horizontal motions along faults, driven by compres-
44 sional and extensional stresses deep within the slab. The compressional part is ori-
45 ented 90 degrees from the subduction direction, which is opposite to the usual com-
46 pression in subduction zones. This unusual direction of compression can be explained
47 by subduction of a thickened and buoyant part of the Pacific plate, known as the Hiku-
48 rangi plateau.

1 Introduction

Complex fault configurations and heterogeneous fault conditions, i.e. stress and strength states, govern earthquake rupture development and propagation (Avouac et al., 2014; Floyd et al., 2016; Elliott et al., 2016; Hamling et al., 2017). Such relations can be inferred from the fault geometry and long-term geodetic observations for shallow active faults (Simons et al., 2002; Williams et al., 2013; Elliott et al., 2016; Arai et al., 2016; Hamling et al., 2017; Hayes et al., 2018; Sippl et al., 2018). However, for intraslab earthquakes occurring below ~ 50 km depth, these physical controlling factors are difficult to assess because of challenges to map structure at such depths, and the general lack of seismicity there (Wiens, 2001; Ranero et al., 2005; Page et al., 2016; Dascher-Cousineau et al., 2020; Gomberg & Bodin, 2021). In particular, the internal stress state and its extensional-compression transition regime are often elusive in subducted slabs, although they directly impact intraslab earthquake occurrence and their faulting styles (Astiz et al., 1988; Ammon et al., 2008; Craig et al., 2014; Romeo & Álvarez-Gómez, 2018; Sandiford et al., 2019, 2020; Ye et al., 2021). Thus, imaging the rupture processes of large, deep intraslab earthquakes offers a rare window to investigate the slab configuration, and to understand fault interaction and rupture evolution of these earthquakes, illuminating heterogeneous stress fields.

An intraslab moment magnitude (M_W) 7.3 earthquake occurred offshore the East Cape in northern New Zealand on 4th March 2021, which was followed ~ 4 hours later by a series of the M_W 7.4 and M_W 8.1 earthquakes in the Kermadecs (~ 900 km to the north) (GeoNet, 2021). The M_W 7.3 2021 East Cape earthquake, which is the focus of this paper, may offer insight into the regional slab geometry because of its location and complex rupture process. The 2021 East Cape earthquake locates at the boundary between the southern end of Kermadec trench and the northern end of Hikurangi margin, where the Pacific plate subducts beneath the Australian plate and its convergence decreases and progressively rotates to oblique motion toward the south (Fig. 1) (Collot et al., 1996, 2001; Lewis et al., 1998; Wallace et al., 2009). The earthquake produced observable tsunami signals at tide gauges at the northern coast of New Zealand (GeoNet News, 2021), indicating seafloor deformation due to possible shallow slip. However, the reported centroid depth of the earthquake was ~ 50 km (U.S. Geological Survey Earthquake Hazards Program, 2017; Duputel et al., 2012; Dziewonski et al., 1981; Ekström et al., 2012), and the focal mechanism indicates oblique-thrust motion, with the compressional axis oriented towards the north-south direction (Fig. 1) (U.S. Geological Survey Earthquake Hazards Program, 2017; Duputel et al., 2012; Dziewonski et al., 1981; Ekström et al., 2012). This compressional axis suggests the earthquake

85 was not a simple shallow normal- or reverse-faulting event with the strike angle ori-
86 ented parallel to the trench axis, as is typically seen in many subduction zones (Fig.
87 1) (U.S. Geological Survey Earthquake Hazards Program, 2017; Duputel et al., 2012;
88 Dziewonski et al., 1981; Ekström et al., 2012). All these apparently inconsistent ob-
89 servations (GeoNet, 2021; GeoNet News, 2021) suggest a complex rupture process of
90 the East Cape earthquake, possibly involving multiple faults at different depths.

91 Although the subduction-related deformation processes in the region south of
92 East Cape have received a lot of scientific attention (e.g., Eberhart-Phillips & Reyn-
93 ersons, 1999; Reyners et al., 2006; Wallace et al., 2009; Mochizuki et al., 2021), the tran-
94 sition to the Tonga-Kermadec arc is less well understood. In the region north of East
95 Cape, sporadic deep seismicity (>80-km depth) contrasts with abundant shallow seis-
96 micity (<50-km depth) (Dziewonski et al., 1981; Ekström et al., 2012; GeoNet Moment
97 Tensors, 2021; U.S. Geological Survey Earthquake Hazards Program, 2017; GeoNet,
98 2021). Most of the shallow earthquakes are normal faulting events within the top of
99 the oceanic plate due to trench-normal extensional stress due to slab bending into the
100 trench (Reyners & McGinty, 1999; Henrys et al., 2006; Bassett et al., 2010). With these
101 shallow earthquakes, the plate interface and the surrounding materials have been im-
102 aged down to ~20 km depth (Davey et al., 1997; Bell et al., 2010; Bassett et al., 2010,
103 2016), but the lithospheric structure of the deep slab is poorly resolved. The appar-
104 ent complex rupture process of the 2021 East Cape earthquake offers a unique op-
105 portunity to infer the stress regime associated with the deeper subduction process.

106 Here we show that the rupture process of the 2021 East Cape earthquake involves
107 multiple rupture episodes, that can be fitted with a mixture of reverse, strike-slip, and
108 normal faulting mechanisms. These episodes ruptured multiple faults through the sub-
109 ducted oceanic lithosphere at various depths. The earthquake initiated at approximately
110 70 km depth with an unexpected trench-parallel compressional reverse faulting mech-
111 anism, and followed by a slip episode at about 30 km depth, which is likely governed
112 by more usual slab-bending trench-normal down-dip extension. Such a rupture pro-
113 cess reflects a heterogeneous stress regime within the subducted slab, in response to
114 a possible geometric change of the slab in depth due to either the subduction of a seamount
115 associated with the Ruatoria debris slide (Lewis et al., 1998; Collot et al., 2001; Lewis
116 et al., 2004), or a sharp change in slab buoyancy at the northern end of the subduct-
117 ing Hikurangi oceanic plateau.

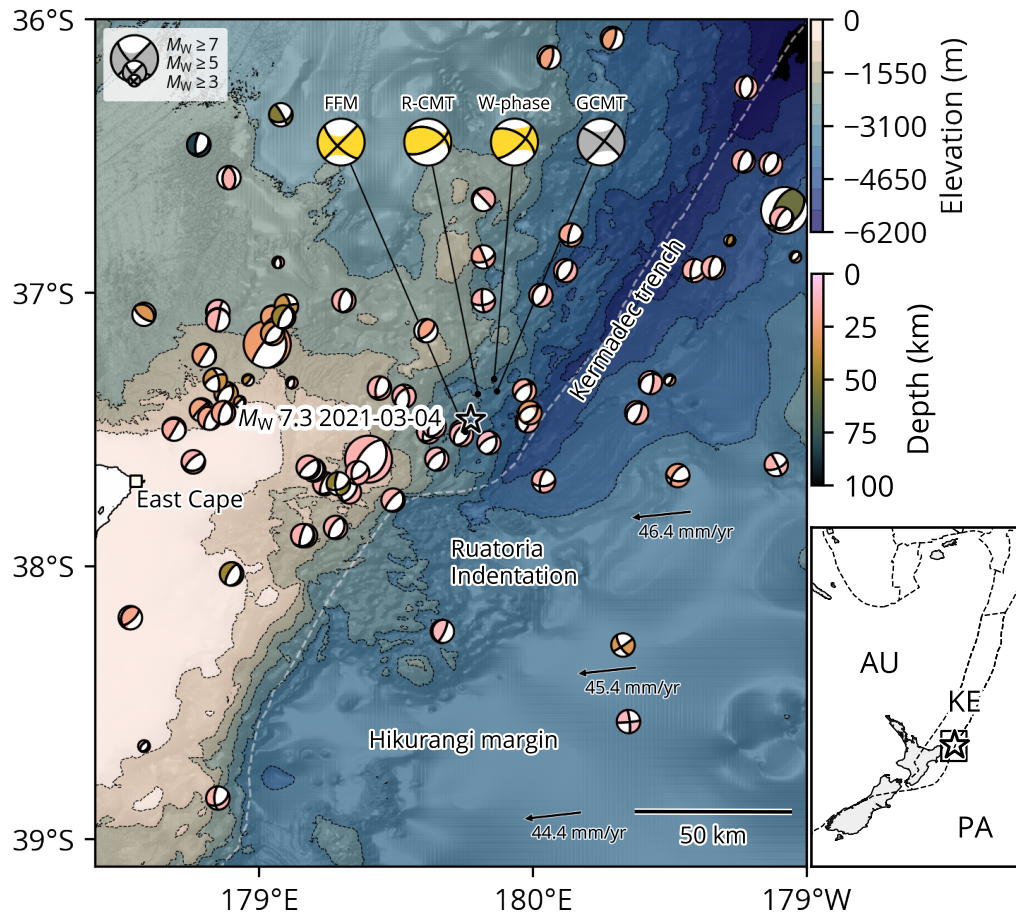


Figure 1. Seismo-tectonic overview of the study region in the north of East Cape, New Zealand. The star shows the relocated hypocenter of the M_W 7.3 2021 East Cape earthquake. Beach balls are the lower-hemisphere stereographic projection of the moment tensor solutions before the 2021 East Cape earthquake, colored by depth (Dziewonski et al., 1981; Ekström et al., 2012). Yellow beach balls are the moment tensor solutions for the 2021 East Cape earthquake obtained by this study (FFM; Finite-fault model, R-CMT; regional centroid moment tensor, W -phase; W -phase moment tensor). Background contours display the bathymetry (Mitchell et al., 2012). The arrows show the relative plate motions with the convergence rate of the Pacific plate (PA) towards the fixed Australian plate (AU) (DeMets et al., 2010). The dashed line gives the approximate location of the subduction trench (e.g., Bassett et al., 2010). The right map shows the wider setting of the study region. The rectangle shows the area of the left map. The star marks the epicenter. The dashed lines are the plate boundaries (Bird, 2003) between the Pacific (PA), the Australian (AU) and the Kermadec (KE) plates.

118 2 Hypocenter, aftershock relocation, and initial source estimates

119 We first determined the hypocenter of the East Cape earthquake by non-linear
120 inversion of P - and S -wave arrival times at regional distances using a 1D velocity model
121 appropriate for the region north of East Cape (Text S1; Fig. S1). Our relocated epi-
122 center lies along the trench axis, and is within 10 km of the GeoNet solution (GeoNet,
123 2021), and ~ 35 km ENE of the U.S. Geological Survey National Earthquake Informa-
124 tion Center (USGS-NEIC) solution (U.S. Geological Survey Earthquake Hazards Pro-
125 gram, 2017) which is consistent with the USGS-NEIC epicenters being systematically
126 shifted to the down-dip direction in subduction zones (e.g., Ye et al., 2017). Our maximum-
127 likelihood hypocenter depth is 72 km. Although this hypocenter depth may be thought
128 to be inherently uncertain due to the sub-optimal station coverage, it provides an ini-
129 tial hypothesis for testing our results of the more complex rupture configuration later.
130 If we instead fix our hypocentral depth at the fixed GeoNet/USGS estimates of 10–
131 12 km (GeoNet, 2021; U.S. Geological Survey Earthquake Hazards Program, 2017),
132 the root-mean-square (RMS) residual of arrival times at the closest stations (<200 km)
133 increases by 0.3 s. Although the deeper hypocentral depth led to lower RMS value,
134 the lower RMS value only represents a better data fit and does not reduce the nonunique-
135 ness of the inverse problem, hence not equivalent to location uncertainty itself. The
136 68% confidence ellipsoid of our solution corresponds to an epicentral uncertainty of
137 0.03° and 0.02° in longitude and latitude, respectively; the depth uncertainty is ± 9
138 km (Fig. S1). However, no depth phases were reported in the International Seismo-
139 logical Centre Bulletin for this earthquake (International Seismological Centre, 2021),
140 presumably due to interference with the long source-time function.

141 Next, we located aftershocks of the 2021 East Cape earthquake the same way as
142 for the mainshock. We focus on events reported by GeoNet (2021) occurring from March
143 4, 2021 to April 11, 2021 (1 week from the mainshock); (Fig. S2), which yields 622
144 events with magnitudes ranging from 1.5–6.2. To assure the robustness of the solu-
145 tions, we remove earthquakes and their arrivals that: (1) were not manually reviewed
146 by GeoNet (2021), (2) have maximum azimuthal gaps of more than 295 degrees, and
147 (3) have fewer than at least 10 phase arrivals (Fig. S2). The median depth uncertainty
148 of these aftershocks is 22 km (with 6 km standard deviation), and the median epicen-
149 tral uncertainties are 0.05° and 0.08° in latitude and longitude, respectively. The af-
150 tershocks suffer large depth uncertainty due to their location outside of the regional
151 network, which hampers an unambiguous determination of the total rupture area. How-
152 ever, we broadly identify both shallow (<30 km) and deep (>50 km) aftershocks, and

153 such a depth distribution could be explained by our preferred rupture model of both
154 shallow and deep ruptures in the downgoing lithosphere.

155 Using a Bayesian bootstrapping centroid-moment tensor (CMT) inversion of low-
156 frequency (2.0–8.5 mHz) teleseismic waveforms for a single-point source (Text S2),
157 we find a mean centroid depth of 53 km, with a centroid position shifted 18 km NNE
158 of our relocated epicenter, and time shift from the origin time of +5 s (Fig. S3). How-
159 ever, the CMT solution has a large non-double couple component (DC=15%). Such
160 a low DC component is likely caused by geometric complexities of the earthquake that
161 may involve multiple faults within the subducted Pacific plate near the Hikurangi trench.

162 Finally, to test the hypothesised rupture complexity, we investigated the rupture
163 process of the earthquake with a multi-point centroid moment tensor (R-CMT) inver-
164 sion method using regional seismic waveforms (Text S3; Figs. S4 to S6). The approach
165 can resolve the first-order features of a complex rupture with few assumptions. The
166 later part of the <25 s period surface waves on the horizontal components at stations
167 within ~400 km epicentral distance are poorly fit (Figs. S5 and S6) due to basin res-
168 onance effects (Kaneko et al., 2019). We find that the East Cape event can be best ex-
169 plained by two sub-events, with the largest sub-event ($M_W \sim 7.3$) at 50–70 km depth
170 occurring 8–10 s after the origin time, and the second sub-event at 7–12 km depth
171 and 6–8 s after the first sub-event. The second sub-event significantly increases wave-
172 form variance reduction by 16–23%. The first sub-event has an oblique-reverse mech-
173 anism. Conversely, the second sub-event has a normal faulting mechanism. Overall,
174 our R-CMT solution corroborates a complex rupture scenario involving at least two
175 sub-events separated by ~40 km in depth: one in the top of the Pacific plate, the other
176 deep within the slab.

177 **3 Intermittent complex multiple rupture episodes with various focal mechanisms**

178 To better understand the rupture development, we applied a finite-fault potency-
179 density inversion method (Shimizu et al., 2020) to estimate the rupture evolution of
180 the 2021 East Cape earthquake (Text S4). The method can flexibly accommodate mul-
181 tiple faults with different geometries rupturing during the same event, which are in-
182 ferred from the spatiotemporal distribution of five-basis double-couple components
183 of the potency-density tensors (Kikuchi & Kanamori, 1991; Ampuero & Dahlen, 2005).
184 In our inversion formulation, the model parameters are objectively determined by min-
185 imizing Akaike’s Bayesian Information Criterion (ABIC) (Akaike, 1980; Yabuki & Matsu’ura,
186 1992), and we do not adopt non-negative constraints for slip vectors. Such a proce-
187 dure can effectively prevent over- or under-smoothing of the source model as theo-

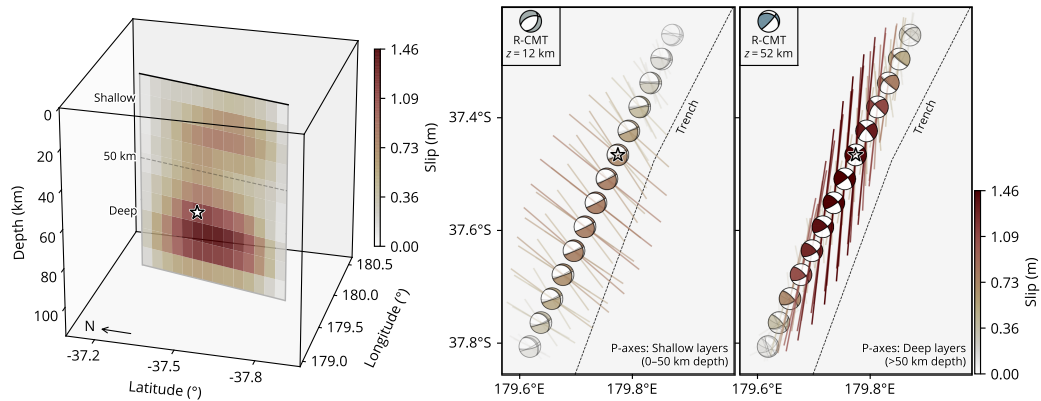


Figure 2. Static slip distribution. The left panel shows the total slip distribution in a 3D view, viewed from the south-west. The star represents our hypocenter. The black line shows the top of the model fault. The right panels show the map view of the slip distribution from shallow (<50 km) and deep depths (≥ 50 km), with beach balls representing double-couple components of the moment tensor solution (Fig. S7), and corresponding P-axis azimuths (bars scaled by slip). The moment tensor is calculated by integrating the slip-rate function for each basis component of moment tensor with respect to time at each sub-fault. The P-axis azimuth is extracted from the resultant double-couple solution for each sub-fault, which is represented by a lower-hemisphere stereographic projection. We show the beach balls from the slip patch corresponding to the fault element with the maximum slip within each given depth range. The inset shows the corresponding R-CMT solutions annotated with their depths (z). The dashed line is the subduction trench (Bird, 2003).

188 retically shown in Fukuda and Johnson (2008). Particularly, we flexibly solve the po-
189 tency density in a finite-fault domain instead of regularizing the model with possi-
190 ble inaccurate subjective assumptions (e.g., positivity constraints, and the prescribed
191 fault geometry). The method has proven effective at resolving complex earthquake rup-
192 tures in a variety of tectonic settings (Shimizu et al., 2020, 2021; Okuwaki et al., 2020;
193 Hicks et al., 2020; Tadapansawut et al., 2021; Yamashita et al., 2021). In practice, we
194 parametrize a 2D vertical model domain along a 200° strike extending from 7- to 107-
195 km depth with a total of 140 source elements (sub-faults) (Fig. 2). This parameter-
196 ization is guided by the observed cluster of the near-trench-parallel aftershocks (Fig.
197 S2). Although it is difficult to resolve the absolute locations of slip surfaces due to in-
198 sufficient spatial resolution of the teleseismic body waves used in our finite-fault mod-
199 eling, in the 2D model domain, we solve the fault-normal and shear-slip vectors at each
200 source element, which are independent of the model domain geometry. In other words,
201 we solve for distributed sources in the model domain that may have any type of fault-
202 ing mechanism required by the data. The model domain therefore allows multiple fault-
203 ing episodes of the earthquake and does not necessarily indicate a single fault plane
204 cutting through the lithosphere in a continuous rupture. Our preferred slip model sug-
205 gests that the earthquake initiated at 72 km depth (Fig. S12), which yields variance
206 reduction (VR) of waveform fitting 74%, corroborating the relocated hypocenter and
207 the R-CMT solution. We test possible model domain geometries that only cover some
208 specific depths, but the finite-fault models of such model setups cannot adequately
209 explain the observed waveforms (Fig. S12). We note that a 3-D parameterization would
210 have been ideal for imaging this earthquake, but it is currently infeasible due to com-
211 putational limits.

212 To further test our model, we also use the same dataset and model domain to
213 invert a finite-fault model but restrict the subfaults to have the same strike and dip
214 (Fig. S14). The results of our test show that in comparison to our preferred finite-fault
215 model, fixing the focal mechanisms to the prescribed model plane has a much lower
216 VR of 25%. This exercise highlights the importance of permitting a complex rupture
217 scenario when modeling this earthquake and shows that an overly simplified model
218 would fail to explain even the first few seconds the direct P waves (for example, first
219 5 s P waves of XMAS and CRZF stations). These early P waves are unlikely to be af-
220 fected by water phases given the source depth. The water multiples should be inco-
221 herent with azimuth, given the variation in water depth around the source region. Such
222 incoherent phases, that are not represented in the Green's functions used in our in-
223 version, cannot translate into complexity in source time function. We also note that
224 using a 1D velocity model for Green's functions without considering the simplifica-

225 tion effects may introduce erroneous biases. Further, even using 3D velocity models
226 to compute the Green's functions, the fidelity of the velocity models remains a source
227 of uncertainty. For example, the local 3D velocity model (e.g., Eberhart-Phillips et al.,
228 2010, 2020) may suffer uncertainties for the area near the 2021 event because of a lack
229 of offshore stations for tomographic inversions. Our approach can address such assumption-
230 induced errors. We explicitly consider these effects by introducing an uncertainty term
231 of the Green's function into the data covariance matrix in the inversion formulation
232 (Yagi & Fukahata, 2011). Such an approach has proven effective in reducing solution
233 errors that are due to model oversimplifications (Yagi & Fukahata, 2011; Minson et
234 al., 2013; Duputel et al., 2014; Ragon et al., 2018).

235 Our preferred finite-fault model suggests that most slip occurred at 55 to 100
236 km depth and ~ 15 km south of the hypocenter, releasing 69% of the total moment
237 (Fig. 2). Another patch of slip is observed at 20–40 km depth, much shallower than
238 the hypocentral depth and comprising 31% of the total moment. The deeper slip is
239 dominated by an oblique strike-slip faulting mechanism. The shallow slip involves
240 a mixture of normal and strike-slip faulting mechanisms. The finite-fault model leads
241 to a moment estimate of 1.7×10^{20} Nm (M_W 7.4). We evaluated the robustness and
242 uncertainty of the finite-fault model by performing synthetic tests (Fig. S13). The re-
243 sult shows that both the slip pattern and the variation of faulting mechanism in the
244 model domain are well reproduced. We will discuss in detail in a later section, but
245 the focal mechanisms of the shallow and deep domains agree with the R-CMT solu-
246 tions (Fig. 2), which show shallow normal faulting with the likely fault plane strik-
247 ing parallel to the trench axis and deep reverse faulting with the compressional axis
248 orienting along the trench axis.

249 The rupture process of the East Cape earthquake involved deep- and shallow-
250 slip corresponding to different faulting types, which may be expressed as a few bursts
251 of rupture episodes (e.g., E1 to E4). In this interpretation, the earthquake initiated as
252 reverse faulting with a strike-slip component for the first 5 s (E1, Fig. 3). The rup-
253 ture then propagated towards the south at 60–100 km depth, releasing 20% of the to-
254 tal moment and lasting for about 5 s (E2, Fig. 3). This episode was dominated by re-
255 verse faulting. The third episode (E3) simultaneously might have ruptured several fault
256 patches from 5 s to 15 s, including a shallow patch at ~ 25 km depth and a deep patch
257 ~ 70 km depth (Fig. 3). The shallow part of E3 ruptured with a normal faulting mech-
258 anism, while the deep patch of E3 had a strike-slip mechanism. The last major episode
259 (E4) ruptured a fault patch beneath the hypocenter for about 5 s with a dominant strike-
260 slip focal mechanism (Fig. 3). We note that E4 is unique as its dominant mechanism

261 suggests a strike-slip faulting style, whilst the E1 and E2 show reverse mechanisms
262 (Fig. 3). The remaining 26% of the total moment was released by slips at both shal-
263 low and deep regions, and the earthquake lasted for about ~ 30 s. Most of the seis-
264 mic moment was released within ~ 20 s in our finite-fault solution, consistent with the
265 half-duration of the GCMT solution (10 s) (Dziewonski et al., 1981; Ekström et al.,
266 2012), which seems typical as for other similar sized earthquakes (e.g., Duputel et al.,
267 2013).

268 The four rupture episodes appear compact in size and seem to involve multi-
269 ple faulting mechanisms at different depths. Given the varying focal mechanisms, the
270 chaotic episodes likely do not result from the same continuous rupture front, but more
271 likely represent segmented slip on different faults that may have interacted with, and
272 triggered, each other.

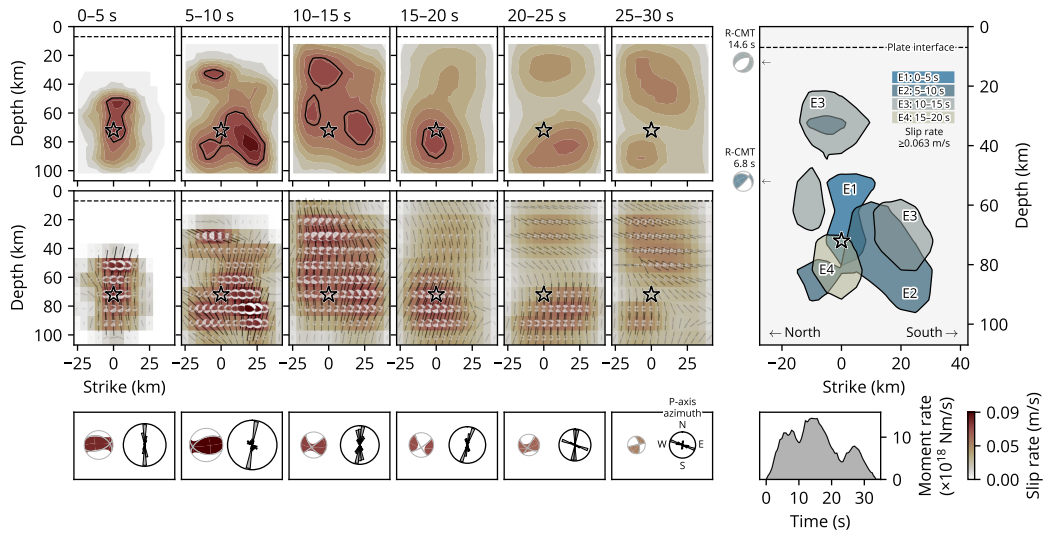


Figure 3. Slip evolution. The left panels show the cross sections of the spatio-temporal distribution of slip rate and the resultant moment-rate tensor solution, given in 5 s long windows. The moment tensor is calculated by integrating the slip-rate function for each basis component of moment tensor with respect to the corresponding time window at each sub-fault. The star represents the hypocenter. The dashed line is the top of the subducting plate (Bassett et al., 2010). The black contour highlights faster slip rates (≥ 0.063 m/s; $\geq 70\%$ of maximum slip rate). The centroid moment tensor for each time window is shown at the bottom, together with the rose diagram of P-axis azimuths weighted by slip rate. The centroid moment tensor is calculated by integrating the slip-rate function for each basis component of moment tensor of all the sub-faults with respect to the corresponding time window and then constructing a final moment tensor from the integrations by spatially integrating the moment tensors from all the subfaults. All the beach balls of the moment-tensor solution are represented as a lower-hemisphere stereographic projection, not rotated according to the model geometry, but in map view. The right panel summarizes the slip-rate evolution. The color for each episode (E1 to E4) corresponds to the time window. The minor slip-rate events within the final two time windows (20–30 s) are not slipping fast enough to plot a contour on the right panel. R-CMT solutions are also shown at the corresponding depths, with their time shift given relative to the hypocentral time. The right-bottom inset is the total moment-rate function from the finite-fault model.

273 Our preferred finite-fault solution suggests a non-uniform moment release of the
274 earthquake, which could be due to spatiotemporally disconnected rupture episodes
275 (Figs. 3 and S15). Alternatively, the results could also represent two sub-events with
276 longer durations. In this case, the deep sub-event initiates at the hypocenter and prop-
277 agates toward south at <2.5 km/s until 15 s from the origin. The higher slip rate, seen
278 during 15–20 s located around the hypocenter, can be a result of faster <5 km/s back-
279 propagation from south to north. The shallow sub-event can be rather a continuous
280 rupture propagating from deep (50 km) to shallow (30 km) depths during 0–15 s at
281 a speed of <2 km/s.

282 **4 Intraslab stress rotation in depth**

283 The source process of the 2021 East Cape earthquake could be characterized as
284 multiple episodes rupturing from deep to shallow within the subducted slab (Fig. 2).
285 The multi-fault rupture may have caused the small double-couple percentage in the
286 moment tensor solution for the 2021 East Cape earthquake (e.g., 32% in the GCMT
287 solution), which is particularly evident for the deeper rupture domain in our finite-
288 fault solution (Figs. 3 and S7). Such a rupture process would involve a mixture of re-
289 verse and strike-slip displacement, which is akin to the 2000 M_W 7.9 Enggano intraslab
290 earthquake that ruptured multiple faults at a similar depth leading to a 33% double-
291 couple component in its GCMT solution (Abercrombie et al., 2003). For the shallow
292 slip episode of the 2021 East Cape earthquake, its focal mechanism shows a mixture
293 of the normal faulting with a strike-slip component. The general trend of the after-
294 shock distribution (Fig. S2) suggests that the fault plane striking toward the northeast-
295 southwest direction likely ruptured during the later phase of the earthquake. Although
296 the limited station azimuth coverage could cause an artificially elongated aftershock
297 distribution, the major axis of the uncertainty ellipse of the mainshock relocation, which
298 shares the similar station coverage, is oriented W-E rather than SW-NE (Fig. S1). It
299 is noteworthy that some aftershocks (U.S. Geological Survey Earthquake Hazards Pro-
300 gram, 2017; Dziewonski et al., 1981; Ekström et al., 2012; GeoNet Moment Tensors,
301 2021) share similar focal mechanisms to the shallow rupture episode (Fig. S8). Given
302 the near-trench location of the East Cape earthquake, there is some ambiguity regard-
303 ing the exact faulting configuration. However, the aftershock distribution indicates
304 that the shallow slip episode likely ruptured a normal fault within the downgoing plate.
305 Additionally, in the absence of clear shallow slip with a reverse-faulting mechanism,
306 this normal faulting episode likely caused the observed tsunami.

307 The varying focal-mechanisms of the four slip episodes (E1–E4) show the com-
308 pressional stress orientation (the P-axis orientation) of the East Cape earthquake ro-
309 tated from the northwest-southeast direction to the north-south direction with a gap
310 in slip and approximate stress transition depth at ~ 50 km (Figs. 2 and 3). The nor-
311 mal faults of the shallow slip episodes striking northeast-southwest agree well with
312 the extension in the upper part of the subducted plate due to the expected plate bend-
313 ing and pulling process (e.g., Astiz et al., 1988; Ammon et al., 2008; Craig et al., 2014;
314 Romeo & Álvarez-Gómez, 2018; Sandiford et al., 2020). Such a bending process seems
315 to have caused most of the background seismicity in this region, which has predom-
316 inant normal faulting mechanisms (Fig. 1; Reyners & McGinty, 1999; Bassett et al.,
317 2010). If the deep slip at 50–100-km depth during the East Cape earthquake was driven
318 by the same bending-related process, we would expect a trench-normal P-axis orien-
319 tation, which is typical for similar events at other subduction zones, where deep trench-
320 parallel reverse faulting is observed (e.g., Okada & Hasegawa, 2003; Ohta et al., 2011;
321 Ye et al., 2012; Todd & Lay, 2013; Ye et al., 2021). However, the deep slip patches of
322 the East Cape earthquake (E1 and E2, and R-CMT Sub-event 1) have oblique-thrusting
323 mechanisms, resulting in a trench-parallel compression. This perplexing P-axis ori-
324 entation indicates an additional regional factor that may have modulated the rupture
325 process of the East Cape earthquake.

326 The interactivity between various faulting episodes is a puzzling part of the East
327 Cape earthquake. Subduction zone earthquakes may involve multiple disconnected
328 subevents with different faulting types that can trigger and interact with each other
329 (Ammon et al., 2008; Lay et al., 2013; Hicks & Rietbrock, 2015; Lay et al., 2020). For
330 the East Cape earthquake, our preferred finite-fault model does not show a contin-
331 uous rupturing path from the deep to shallow episodes (Figs. 2 and 3). The shallow
332 rupture E3 is separated by ~ 40 km from the deep episodes and started ~ 5 s later (Fig.
333 3), suggesting an apparent rupture speed of ~ 8 km/s if the rupture was continuous.
334 Such a rupture speed would be close to the local P -wave speed (Table S1), which is
335 unlikely. More likely, slip episodes E1 and E2 triggered the following shallow episode
336 E3 due to either the static and/or dynamic stress change from the initial deep rup-
337 ture. A stress transition or strength contrast within the slab can work as an inhom-
338 ogeneous barrier (Das & Aki, 1977; Aki, 1979) to smooth propagation from deep to shal-
339 low rupture during the East Cape earthquake. Therefore, the rupture evolution of the
340 earthquake may have developed as discontinuous jumps by means of stress trigger-
341 ing (Miyazawa & Mori, 2005; Sleep & Ma, 2008; Fischer, Sammis, et al., 2008; Fischer,
342 Peng, & Sammis, 2008) across the apparent stress/strength barrier between the deep
343 and shallow rupture areas.

344 Large intraplate earthquakes within the downgoing plate in subduction zones
345 are typically caused either by the down-dip bending and unbending of the slab (e.g.,
346 Astiz et al., 1988; Craig et al., 2014; Sandiford et al., 2020), the reactivation of ma-
347 jor oceanic fabrics, including fracture zones (e.g., Abercrombie et al., 2003; Meng et
348 al., 2012; Yue et al., 2012), or the tearing of the slab (e.g., Tanioka et al., 1995). How-
349 ever, the orientation and rupture complexity of the 2021 East Cape event deviates from
350 these typical events. Two events with apparently similar deep trench-parallel com-
351 pression in the slab include 2000 M_W 7.9 Enggano and 2009 M_W 7.6 Padang earth-
352 quakes, offshore Sumatra (Abercrombie et al., 2003; Wiseman et al., 2012). However,
353 these events likely ruptured pre-existing fabrics in the downgoing plate (Abercrombie
354 et al., 2003), such as fracture zones (Wiseman et al., 2012). Both earthquakes poten-
355 tially represent the continuation of the diffuse deformation within the Wharton basin,
356 and both consistently ruptured orthogonal fabrics toward the top of the downgoing
357 plate both updip and downdip from the trench, where highly oblique convergence in-
358 herently causes a rotated state of the stress in the slab. In contrast, the 2021 East Cape
359 earthquake, which occurred deeper beneath the top of the slab, does not align with
360 the expected oceanic fabric, and is not obviously part of a wider, plate-scale, defor-
361 mation field, where there is no obvious oblique convergence nor are fracture zones
362 of an orientation consistent with the observed mechanisms subducted (Fig. 1). Instead,
363 the rupture processes may represent a unique case, highlighting a different type of
364 stress transition within the subducted slab.

365 **5 A contorted slab structure due to slab buoyancy variations?**

366 A key question is why does this part of the Hikurangi subduction zone exhibit
367 an atypical stress regime, as manifested in the rupture process of the 2021 East Cape
368 earthquake? Slab models of this region (Hayes, 2018; Hayes et al., 2018; Williams et
369 al., 2013) show a homogeneous planar structure (Fig. S9) which would be expected
370 to lead to a trench-normal compression in the deeper part of the slab. However, these
371 slab models are poorly constrained near the East Cape earthquake, largely because of
372 a lack of plate interface thrust earthquakes in the region (Fig. 1). The rupture pro-
373 cess of the East Cape earthquake therefore potentially offers new insight into the lo-
374 cal slab structure.

375 One possible explanation is that the slab surface warps downward north of the
376 hypocenter, forming a depression at the plate interface (Fig. 4). The warping is likely
377 a response to the buoyancy gradients in the subducting plate, which allows the less
378 buoyant parts of the slab to sink more rapidly than the buoyant parts. The internal

379 stress field from such a slab topology would be complex, leading to strong 3-D stress
380 rotations around the localized downwarp in a manner as shown in the 2021 East Cape
381 earthquake (Fig. 2). One contribution to the buoyancy gradients might be the sub-
382 duction of a large-scale seamount. About 30 km south-west from the epicenter, the
383 Quaternary Ruatoria seamount was obliquely subducted at the margin (Lewis et al.,
384 1998; Collot et al., 2001; Lewis et al., 2004), forming the characteristic bathymetry of
385 the Ruatoria indentation (Fig. 1). The Ruatoria seamount could deflect and bend the
386 slab, causing the intraslab stress state to rotate from trench-normal compression to
387 trench-parallel compression across the hypocentral area. Numerical models of slab
388 stress in the presence of subducted buoyant features in the oceanic plate support such
389 a stress rotation and lateral spreading mechanism (e.g., Mason et al., 2010). Trench-
390 parallel compression has also been seen in other parts of the Hikurangi subduction
391 zone, for example, Reyners and McGinty (1999) and McGinty et al. (2000) observed
392 some strike-slip seismicity with a trench-parallel compression component, which are
393 beneath or close to the shoreline of the Raukumara Peninsula. Although these earth-
394 quakes should reflect the stress state once the plate is already subducted, it is pos-
395 sible they reflect stress heterogeneity due to pervasive seamount subduction along the
396 northern Hikurangi subduction zone (Barker et al., 2009).

397 An alternative explanation may arise from the location of the East Cape earth-
398 quake with respect to the transition between the Kermadec trench and Hikurangi mar-
399 gin, marked by the edge of the Hikurangi plateau, which is represented by a clear bathy-
400 metric scarp running along its northern boundary (Davy & Collot, 2000). This tran-
401 sition from the subduction of normal oceanic lithosphere to the north, to the subduc-
402 tion of the thickened oceanic crust associated with the igneous Hikurangi plateau likely
403 leads to a pronounced, short-wavelength flexural warping at the plateau edge. The
404 superposition of this N-S flexural stress field in conjunction with the down-dip bend-
405 ing stress field could have produced a complex pattern that varies at short-length scales
406 within the subducted slab. Such a heterogeneous stress field may have regulated the
407 rupture process of the East Cape earthquake. The sporadic background seismicity north
408 of the 2021 source region (Fig. S16) might also result from such a complex stress field.
409 It is noteworthy that in 2001, ~80 km northeast of the 2021 event, there was a M_W
410 7.1 earthquake deep in the Pacific plate (~60 km depth) showing a reverse faulting
411 mechanism with its P-axis oriented perpendicular to the Kermadec trench (Fig. S8),
412 which was likely driven by conventional trench-normal down-dip compression. This
413 earthquake suggests that flexural warping due to the subducting Hikurangi plateau
414 does not extend this far to the north.

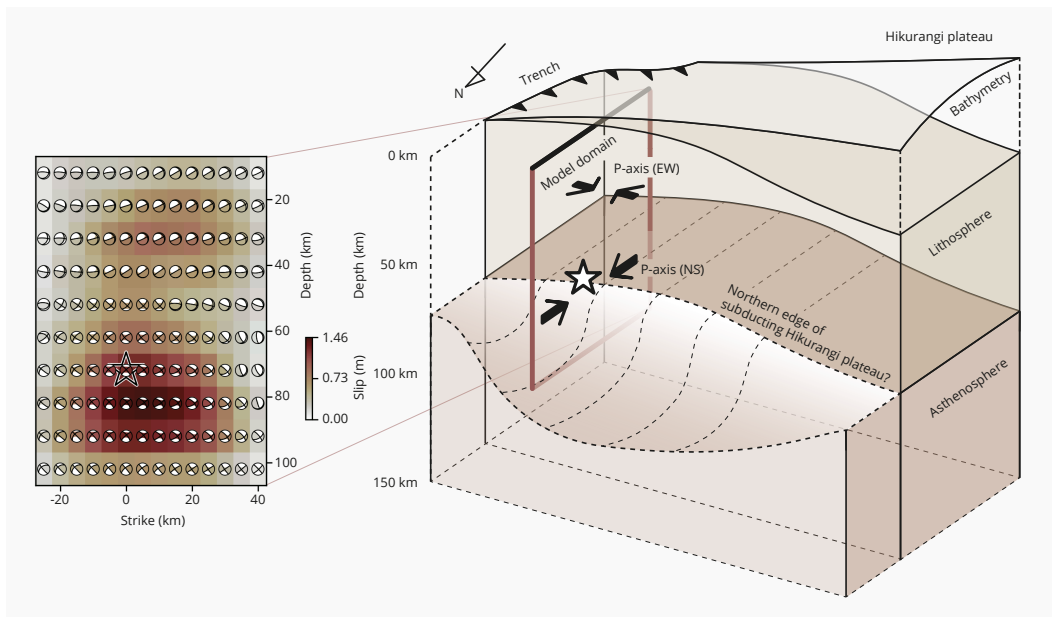


Figure 4. Cartoon interpretation of the inferred slab geometry and stress regimes based on our observations of the 2021 East Cape earthquake. The star shows the hypocenter. The arrow shows the compressional axis. The left panel shows the cross-section of our finite-fault solution (Fig. S7).

415 Whilst there have been many studies on the impact of subducting buoyant fea-
 416 tures on subduction megathrust coupling and interface seismogenesis (e.g., Wang &
 417 Bilek, 2011; Nishikawa & Ide, 2014), there have been far fewer studies that have con-
 418 sidered their impact on intraslab seismicity. The rarity of deep intraslab earthquakes
 419 in the northern Hikurangi subduction zone makes it difficult to distinguish between
 420 the seamount and plateau models of stress rotation. However, it is also possible that
 421 both features play a concurrent role, with stress rotations superimposed from both.

422

423 6 Conclusions

424 We determined the rupture geometry of the 2021 M_W 7.3 East Cape, New Zealand
425 earthquake using a novel finite-fault inversion technique. Our method does not re-
426 quire a-priori knowledge of the fault geometry and can flexibly resolve complex fault-
427 ing styles in large earthquakes. Therefore, it can illuminate the heterogeneous stress
428 state near the earthquake. We show that the East Cape earthquake involves deep- and
429 shallow-slip episodes, likely rupturing multiple faults with various faulting styles. We
430 find distinct rupture episodes within the shallow (~ 30 km) and deep (~ 70 km) parts
431 of the subducted oceanic plate, with distinct mechanisms of normal and a mixture of
432 strike-slip and reverse faulting, respectively. The deep and shallow faulting episodes
433 likely result from the superposition of depth-varying slab bending stress with more
434 localized trench-parallel lateral variations in flexural stresses. The rotation of P-axes
435 suggests that the intraplate stress state is locally rotated from trench-normal compres-
436 sion to trench-parallel compression. Such a stress rotation in depth requires the slab
437 geometry to change sharply, which may have been induced by a subducted seamount
438 or the additional buoyancy of the Hikurangi plateau. Our study suggests that under-
439 standing the generation of intermediate and deep intraslab seismicity requires a de-
440 tailed treatment of localized variations in slab geometry caused by the subduction of
441 heterogeneous features, such as ocean plateaus and seamounts.

442 **Acknowledgments**

443 We thank editor Dr. Germán Prieto, associate editor Dr. Ake Fagereng, reviewers Dr.
444 Emily Warren-Smith and Dr. Rachel Abercrombie, and an anonymous reviewer for their
445 evaluations and constructive suggestions. We thank Lingsen Meng, Han Bao, Baon-
446 ing Wu, Richard G. Davy, Lior Suchoy, Fangqin Chen, Rhodri Davies, Tian Feng, Yuqing
447 Xie, Liuwei Xu and Tong Zhou for the discussions. We are also grateful to John Ris-
448 tau for discussions on the original GeoNet moment tensor solutions. TJC was supported
449 in this work by the Royal Society under URF\R1\180088. COMET is the NERC Cen-
450 tre for the Observation and Modelling of Earthquakes, Volcanoes and Tectonics, a part-
451 nership between UK Universities and the British Geological Survey. This work was
452 supported by the Grant-in-Aid for Scientific Research (C) 19K04030. The facilities of
453 IRIS Data Services, and specifically the IRIS Data Management Center, were used for
454 access to waveforms, related metadata, and/or derived products used in this study.
455 IRIS Data Services are funded through the Seismological Facilities for the Advance-
456 ment of Geoscience (SAGE) Award of the National Science Foundation under Coop-
457 erative Support Agreement EAR-1851048. We also thank the GeoNet data centre for
458 making their continuous broadband and strong motion seismic data openly available.
459 The authors declare no conflicts of interest relevant to this study.

460 **Open Research**

461 All the materials presented in this paper are archived and available at [https://doi.org/](https://doi.org/10.5281/zenodo.5720036)
462 [10.5281/zenodo.5720036](https://doi.org/10.5281/zenodo.5720036). All seismic data were downloaded through the IRIS Wilber
463 3 system (https://ds.iris.edu/wilber3/find_event) or IRIS Web Services ([https://service](https://service.iris.edu)
464 [.iris.edu](https://service.iris.edu)), including the following seismic networks: the GT (Global Telemetered Seis-
465 mograph Network (USAF/USGS); Albuquerque Seismological Laboratory (ASL)/USGS,
466 1993); the IC (New China Digital Seismograph Network; Albuquerque Seismological
467 Laboratory (ASL)/USGS, 1992); the IU (Global Seismograph Network (GSN - IRIS/USGS);
468 Albuquerque Seismological Laboratory (ASL)/USGS, 1988); the GE (GEOFON Seis-
469 mic Network; GEOFON Data Centre, 1993); the AU (Australian National Seismograph
470 Network (ANSN); Geoscience Australia (GA), 1994); the HK (Hong Kong Seismograph
471 Network; Hong Kong Observatory, 2009); the G (GEOSCOPE; Institut De Physique
472 Du Globe De Paris (IPGP) & Ecole Et Observatoire Des Sciences De La Terre De Stras-
473 bourg (EOST), 1982); the NZ (New Zealand National Seismograph Network; Institute
474 of Geological & Nuclear Sciences Ltd (GNS New Zealand), 1988; Petersen et al., 2011);
475 the AI (Antarctic Seismographic Argentinean Italian Network - OGS; Istituto Nazionale
476 Di Oceanografia E Di Geofisica Sperimentale, 1992); the II (IRIS/IDA Seismic Network;

477 Scripps Institution Of Oceanography, 1986); the C (Chilean National Seismic Network;
 478 Universidad de Chile Dept de Geofisica (DGF UChile Chile), 1991); the PS (Pacific21
 479 (ERI/STA); University of Tokyo Earthquake Research Institute (Todai ERI Japan), 1989).
 480 We used ObsPy (Beyreuther et al., 2010, <https://doi.org/10.5281/zenodo.165135>), Py-
 481 rocko (The Pyrocko Developers, 2017, <https://pyrocko.org/>), matplotlib (Hunter, 2007,
 482 <https://doi.org/10.5281/zenodo.592536>), Generic Mapping Tools (Wessel & Luis, 2017,
 483 <https://doi.org/10.5281/zenodo.3407865>); and Scientific colour maps (Cramer, 2018;
 484 Cramer et al., 2020, <https://doi.org/10.5281/zenodo.1243862>) for data processing and
 485 visualisation. The NonLinLoc software used for hypocenter relocation is available at
 486 <http://alomax.free.fr/nlloc/>. The Grond software (Heimann et al., 2018) used for W-
 487 phase CMT inversion is available at <https://pyrocko.org/grond/docs/current/>. The
 488 ISOLA software used for R-CMT inversion is available at [http://seismo.geology.upatras](http://seismo.geology.upatras.gr/isola/)
 489 [.gr/isola/](http://seismo.geology.upatras.gr/isola/).

490 References

- 491 Abercrombie, R. E., Antolik, M., & Ekström, G. (2003). The June 2000 Mw 7.9
 492 earthquakes south of Sumatra: Deformation in the India-Australia Plate. *J.*
 493 *Geophys. Res. Solid Earth*, 108(B1), 2018. doi:10.1029/2001jb000674
- 494 Akaike, H. (1980). Likelihood and the Bayes procedure. *Trab. Estad. Y Investig.*
 495 *Oper.*, 31(1), 143–166. Retrieved from <https://doi.org/10.1007/BF02888350>
 496 doi:10.1007/BF02888350
- 497 Aki, K. (1979). Characterization of barriers on an earthquake fault. *J. Geophys. Res.*,
 498 84(B11), 6140. doi:10.1029/JB084iB11p06140
- 499 Albuquerque Seismological Laboratory (ASL)/USGS. (1988). *Global Seismograph*
 500 *Network (GSN - IRIS/USGS)*. International Federation of Digital Seismograph
 501 Networks. doi:10.7914/SN/IU
- 502 Albuquerque Seismological Laboratory (ASL)/USGS. (1992). *New China Digital Seis-*
 503 *mograph Network*. International Federation of Digital Seismograph Networks.
 504 doi:10.7914/SN/IC
- 505 Albuquerque Seismological Laboratory (ASL)/USGS. (1993). *Global Telemetered*
 506 *Seismograph Network (USAF/USGS)*. International Federation of Digital Seis-
 507 mograph Networks. Retrieved from [http://www.fdsn.org/doi/10.7914/SN/](http://www.fdsn.org/doi/10.7914/SN/GT)
 508 [GT](http://www.fdsn.org/doi/10.7914/SN/GT) doi:10.7914/SN/GT
- 509 Ammon, C. J., Kanamori, H., & Lay, T. (2008). A great earthquake doublet and seis-
 510 mic stress transfer cycle in the central Kuril islands. *Nature*, 451(7178), 561–
 511 565. doi:10.1038/nature06521
- 512 Ampuero, J.-P., & Dahlen, F. A. (2005). Ambiguity of the Moment Tensor. *Bull. Seis-*

- 513 *mol. Soc. Am.*, 95(2), 390–400. doi:10.1785/0120040103
- 514 Arai, R., Takahashi, T., Kodaira, S., Kaiho, Y., Nakanishi, A., Fujie, G., ... Kaneda, Y.
 515 (2016). Structure of the tsunamigenic plate boundary and low-frequency
 516 earthquakes in the southern Ryukyu Trench. *Nat. Commun.*, 7, 1–7.
 517 doi:10.1038/ncomms12255
- 518 Astiz, L., Lay, T., & Kanamori, H. (1988). Large intermediate-depth earthquakes
 519 and the subduction process. *Phys. Earth Planet. Inter.*, 53(1-2), 80–166.
 520 doi:10.1016/0031-9201(88)90138-0
- 521 Avouac, J. P., Ayoub, F., Wei, S., Ampuero, J. P., Meng, L., Leprince, S., ... Helm-
 522 berger, D. (2014). The 2013, Mw 7.7 Balochistan earthquake, energetic
 523 strike-slip reactivation of a thrust fault. *Earth Planet. Sci. Lett.*, 391, 128–134.
 524 doi:10.1016/j.epsl.2014.01.036
- 525 Barker, D. H., Sutherland, R., Henrys, S., & Bannister, S. (2009). Geometry of the
 526 Hikurangi subduction thrust and upper plate, North Island, New Zealand.
 527 *Geochemistry, Geophys. Geosystems*, 10(2). doi:10.1029/2008GC002153
- 528 Bassett, D., Kopp, H., Sutherland, R., Henrys, S., Watts, A. B., Timm, C., ... Ronde,
 529 C. E. J. (2016). Crustal structure of the Kermadec arc from MANGO seis-
 530 mic refraction profiles. *J. Geophys. Res. Solid Earth*, 121(10), 7514–7546.
 531 doi:10.1002/2016JB013194
- 532 Bassett, D., Sutherland, R., Henrys, S., Stern, T., Scherwath, M., Benson, A., ... Hen-
 533 derson, M. (2010). Three-dimensional velocity structure of the northern
 534 Hikurangi margin, Raukumara, New Zealand: Implications for the growth of
 535 continental crust by subduction erosion and tectonic underplating. *Geochem-
 536 istry, Geophys. Geosystems*, 11(10). doi:10.1029/2010GC003137
- 537 Bell, R., Sutherland, R., Barker, D. H., Henrys, S., Bannister, S., Wallace, L., & Bea-
 538 van, J. (2010). Seismic reflection character of the Hikurangi subduction
 539 interface, New Zealand, in the region of repeated Gisborne slow slip events.
 540 *Geophys. J. Int.*, 180(1), 34–48. doi:10.1111/j.1365-246X.2009.04401.x
- 541 Beyreuther, M., Barsch, R., Krischer, L., Megies, T., Behr, Y., & Wassermann, J.
 542 (2010). ObsPy: A Python Toolbox for Seismology. *Seismol. Res. Lett.*, 81(3),
 543 530–533. doi:10.1785/gssrl.81.3.530
- 544 Bird, P. (2003). An updated digital model of plate boundaries. *Geochemistry, Geo-
 545 phys. Geosystems*, 4(3), 1105. doi:10.1029/2001GC000252
- 546 Bormann, P. (2012). New Manual of Seismological Observatory Practice (NMSOP-2).
 547 *IASPEI, GFZ Ger. Res. Cent. Geosci.* doi:10.2312/GFZ.NMSOP-2
- 548 Collot, J. Y., Delteil, J., Lewis, K. B., Davy, B., Lamarche, G., Audru, J. C., ... Uruski,
 549 C. (1996). From oblique subduction to intra-continental transpression:

- 550 Structures of the southern Kermadec-Hikurangi margin from multibeam
551 bathymetry, side-scan sonar and seismic reflection. *Mar. Geophys. Res.*, 18(2-4),
552 357–381. doi:10.1007/BF00286085
- 553 Collot, J. Y., Lewis, K., Lamarche, G., & Lallemand, S. (2001). The giant Ruatoria
554 debris avalanche on the northern Hikurangi margin, New Zealand: Result of
555 oblique seamount subduction. *J. Geophys. Res. Solid Earth*, 106(B9), 19271–
556 19297. doi:10.1029/2001jb900004
- 557 Craig, T. J., Copley, A., & Jackson, J. (2014). A reassessment of outer-rise seismicity
558 and its implications for the mechanics of oceanic lithosphere. *Geophys. J. Int.*,
559 197(1), 63–89. doi:10.1093/gji/ggu013
- 560 Crameri, F. (2018). Geodynamic diagnostics, scientific visualisation and StagLab
561 3.0. *Geosci. Model Dev.*, 11(6), 2541–2562. doi:10.5194/gmd-11-2541-2018
- 562 Crameri, F., Shephard, G. E., & Heron, P. J. (2020). The misuse of colour in science
563 communication. *Nat. Commun.*, 11(1), 5444. doi:10.1038/s41467-020-19160-
564 7
- 565 Das, S., & Aki, K. (1977). Fault plane with barriers: A versatile earthquake model. *J.*
566 *Geophys. Res.*, 82(36), 5658–5670. doi:10.1029/JB082i036p05658
- 567 Dascher-Cousineau, K., Brodsky, E. E., Lay, T., & Goebel, T. H. W. (2020). What Con-
568 trols Variations in Aftershock Productivity? *J. Geophys. Res. Solid Earth*, 125(2),
569 e2019JB018111. doi:10.1029/2019JB018111
- 570 Davey, F. J., Henrys, S., & Lodolo, E. (1997). A seismic crustal section across the East
571 Cape convergent margin, New Zealand. *Tectonophysics*, 269(3-4), 199–215.
572 doi:10.1016/S0040-1951(96)00165-5
- 573 Davy, B., & Collot, J. Y. (2000). The Rapuhia Scarp (northern Hikurangi Plateau)
574 - Its nature and subduction effects on the Kermadec Trench. *Tectonophysics*,
575 328(3-4), 269–295. doi:10.1016/S0040-1951(00)00211-0
- 576 DeMets, C., Gordon, R. G., & Argus, D. F. (2010). Geologically current plate mo-
577 tions. *Geophys. J. Int.*, 181(1), 1–80. doi:10.1111/j.1365-246X.2009.04491.x
- 578 Duputel, Z., Agram, P. S., Simons, M., Minson, S. E., & Beck, J. L. (2014). Account-
579 ing for prediction uncertainty when inferring subsurface fault slip. *Geophys. J.*
580 *Int.*, 197(1), 464–482. doi:10.1093/gji/ggt517
- 581 Duputel, Z., Rivera, L., Kanamori, H., & Hayes, G. (2012). W phase source inversion
582 for moderate to large earthquakes (1990-2010). *Geophys. J. Int.*, 189(2), 1125–
583 1147. doi:10.1111/j.1365-246X.2012.05419.x
- 584 Duputel, Z., Tsai, V. C., Rivera, L., & Kanamori, H. (2013). Using centroid time-
585 delays to characterize source durations and identify earthquakes with unique
586 characteristics. *Earth Planet. Sci. Lett.*, 374, 92–100. Retrieved from <http://>

- 587 dx.doi.org/10.1016/j.epsl.2013.05.024 doi:10.1016/j.epsl.2013.05.024
- 588 Dzierwowski, A. M., Chou, T.-A., & Woodhouse, J. H. (1981). Determination of
589 earthquake source parameters from waveform data for studies of global
590 and regional seismicity. *J. Geophys. Res. Solid Earth*, 86(B4), 2825–2852.
591 doi:10.1029/JB086iB04p02825
- 592 Eberhart-Phillips, D., Bannister, S., Reyners, M., & Henrys, S. (2020). *New Zealand*
593 *Wide model 2.2 seismic velocity and Qs and Qp models for New Zealand*. Zenodo.
594 doi:10.5281/zenodo.3779523
- 595 Eberhart-Phillips, D., & Reyners, M. (1999). Plate interface properties in the north-
596 east Hikurangi subduction zone, New Zealand, from converted seismic waves.
597 *Geophys. Res. Lett.*, 26(16), 2565–2568. doi:10.1029/1999GL900567
- 598 Eberhart-Phillips, D., Reyners, M., Bannister, S., Chadwick, M., & Ellis, S. (2010).
599 Establishing a versatile 3-D seismic velocity model for New Zealand. *Seismol.*
600 *Res. Lett.*, 81(6), 992–1000. doi:10.1785/gssrl.81.6.992
- 601 Ekström, G., Nettles, M., & Dzierwowski, A. (2012). The global CMT project
602 2004–2010: Centroid-moment tensors for 13,017 earthquakes. *Phys. Earth*
603 *Planet. Inter.*, 200–201, 1–9. doi:10.1016/j.pepi.2012.04.002
- 604 Elliott, J. R., Jolivet, R., Gonzalez, P. J., Avouac, J. P., Hollingsworth, J., Searle, M. P.,
605 & Stevens, V. L. (2016). Himalayan megathrust geometry and relation to
606 topography revealed by the Gorkha earthquake. *Nat. Geosci.*, 9(2), 174–180.
607 doi:10.1038/ngeo2623
- 608 Fischer, A. D., Peng, Z., & Sammis, C. G. (2008). Dynamic triggering of high-
609 frequency bursts by strong motions during the 2004 Parkfield earthquake
610 sequence. *Geophys. Res. Lett.*, 35(12), L12305. doi:10.1029/2008GL033905
- 611 Fischer, A. D., Sammis, C. G., Chen, Y., & Teng, T.-L. (2008). Dynamic
612 Triggering by Strong-Motion P and S Waves: Evidence from the 1999
613 Chi-Chi, Taiwan, Earthquake. *Bull. Seismol. Soc. Am.*, 98(2), 580–592.
614 doi:10.1785/0120070155
- 615 Floyd, M. A., Walters, R. J., Elliott, J. R., Funning, G. J., Svarc, J. L., Murray, J. R., ...
616 Wright, T. J. (2016). Spatial variations in fault friction related to lithology
617 from rupture and afterslip of the 2014 South Napa, California, earthquake.
618 *Geophys. Res. Lett.*, 43(13), 6808–6816. doi:10.1002/2016GL069428
- 619 Fukuda, J., & Johnson, K. M. (2008). A fully Bayesian inversion for spatial distribu-
620 tion of fault slip with objective smoothing. *Bull. Seismol. Soc. Am.*, 98(3), 1128–
621 1146. doi:10.1785/0120070194
- 622 GEOFON Data Centre. (1993). *GEOFON Seismic Network*. Deutsches Geo-
623 Forschungszentrum GFZ. doi:10.14470/TR560404

- 624 GeoNet. (2021). *GeoNet Earthquake Catalog*. Retrieved from <https://www.geonet.org>
625 [.nz/data/types/eq_catalogue](https://www.geonet.org.nz/data/types/eq_catalogue)
- 626 GeoNet Moment Tensors. (2021). *GeoNet Moment Tensors*. Retrieved from [https://](https://github.com/GeoNet/data/tree/main/moment-tensor)
627 github.com/GeoNet/data/tree/main/moment-tensor
- 628 GeoNet News. (2021). *Friday 5 March Tsunami: What happened and*
629 *what did you see?* Retrieved from [https://www.geonet.org.nz/news/](https://www.geonet.org.nz/news/1gvqV0oHGIULbydSQD8W1Y)
630 [1gvqV0oHGIULbydSQD8W1Y](https://www.geonet.org.nz/news/1gvqV0oHGIULbydSQD8W1Y)
- 631 Geoscience Australia (GA). (1994). *Australian National Seismograph Network*
632 *(ANSN)*. Retrieved from <https://www.fdsn.org/networks/detail/AU/>
- 633 Gomberg, J., & Bodin, P. (2021). The Productivity of Cascadia Aftershock Se-
634 quences. *Bull. Seismol. Soc. Am.*, 111(3), 1–14. doi:10.1785/0120200344
- 635 Hamling, I. J., Hreinsdóttir, S., Clark, K., Elliott, J., Liang, C., Fielding, E., ... Stir-
636 ling, M. (2017). Complex multifault rupture during the 2016 Mw 7.8 Kaikōura
637 earthquake, New Zealand. *Science*, 356(6334). doi:10.1126/science.aam7194
- 638 Hayes, G. P. (2018). *Slab2 - A Comprehensive Subduction Zone Geometry Model: U.S.*
639 *Geological Survey data release*. doi:10.5066/F7PV6JNV
- 640 Hayes, G. P., Moore, G. L., Portner, D. E., Hearne, M., Flamme, H., Furtney, M., &
641 Smoczyk, G. M. (2018). Slab2, a comprehensive subduction zone geometry
642 model. *Science*, 362(6410), 58–61. doi:10.1126/science.aat4723
- 643 Heimann, S., Isken, M., Kühn, D., Sudhaus, H., Steinberg, A., Vasyura-Bathke,
644 H., ... Dahm, T. (2018). *Grond - A probabilistic earthquake source inver-*
645 *sion framework*. Retrieved from <http://pyrocko.org/grond/docs/current/>
646 doi:10.5880/GFZ.2.1.2018.003
- 647 Henrys, S., Reyners, M., Pecher, I., Bannister, S., Nishimura, Y., & Maslen, G. (2006).
648 Kinking of the subducting slab by escalator normal faulting beneath the North
649 Island of New Zealand. *Geology*, 34(9), 777–780. doi:10.1130/G22594.1
- 650 Hicks, S. P., Okuwaki, R., Steinberg, A., Rychert, C. A., Harmon, N., Abercrom-
651 bie, R. E., ... Sudhaus, H. (2020). Back-propagating supershear rupture in
652 the 2016 Mw 7.1 Romanche transform fault earthquake. *Nat. Geosci.*, 13(9),
653 647–653. doi:10.1038/s41561-020-0619-9
- 654 Hicks, S. P., & Rietbrock, A. (2015). Seismic slip on an upper-plate normal fault
655 during a large subduction megathrust rupture. *Nat. Geosci.*, 8(12), 955–960.
656 doi:10.1038/ngeo2585
- 657 Hong Kong Observatory. (2009). *Hong Kong Seismograph Network*. Retrieved from
658 http://www.hko.gov.hk/gts/quake/sp_seismo_network_intro_e.htm
- 659 Hunter, J. D. (2007). Matplotlib: A 2D Graphics Environment. *Comput. Sci. Eng.*,
660 9(3), 90–95. doi:10.1109/MCSE.2007.55

- 661 Institut De Physique Du Globe De Paris (IPGP), & Ecole Et Observatoire Des Sci-
662 ences De La Terre De Strasbourg (EOST). (1982). *GEOSCOPE, French Global*
663 *Network of broad band seismic stations*. Institut de physique du globe de Paris
664 (IPGP), Université de Paris. doi:10.18715/GEOSCOPE.G
- 665 Institute of Geological & Nuclear Sciences Ltd (GNS New Zealand). (1988). *New*
666 *Zealand National Seismograph Network*. Retrieved from [https://www.fdsn.org/](https://www.fdsn.org/networks/detail/NZ/)
667 [networks/detail/NZ/](https://www.fdsn.org/networks/detail/NZ/)
- 668 International Seismological Centre. (2021). *On-line Bulletin*.
669 doi:10.31905/D808B830
- 670 Istituto Nazionale Di Oceanografia E Di Geofisica Sperimentale. (1992). *Antarctic*
671 *Seismographic Argentinean Italian Network - OGS*. International Federation of
672 Digital Seismograph Networks. doi:10.7914/SN/AI
- 673 Kaneko, Y., Ito, Y., Chow, B., Wallace, L. M., Tape, C., Grapenthin, R., ... Hino, R.
674 (2019). Ultra-long Duration of Seismic Ground Motion Arising From a Thick,
675 Low-Velocity Sedimentary Wedge. *J. Geophys. Res. Solid Earth*, 124(10), 10347–
676 10359. doi:10.1029/2019JB017795
- 677 Kennett, B. L., Engdahl, E. R., & Buland, R. (1995). Constraints on seismic ve-
678 locities in the Earth from traveltimes. *Geophys. J. Int.*, 122(1), 108–124.
679 doi:10.1111/j.1365-246X.1995.tb03540.x
- 680 Kikuchi, M., & Kanamori, H. (1991). Inversion of complex body waves-
681 III. *Bull. Seism. Soc. Am.*, 81(6), 2335–2350. Retrieved from [https://](https://pubs.geoscienceworld.org/ssa/bssa/article-abstract/81/6/2335/102472/)
682 pubs.geoscienceworld.org/ssa/bssa/article-abstract/81/6/2335/102472/
683 [Inversion-of-complex-body-waves-III](https://pubs.geoscienceworld.org/ssa/bssa/article-abstract/81/6/2335/102472/)
- 684 Laske, G., Masters, T. G., Ma, Z., & Pasyanos, M. (2013). Update on CRUST1.0
685 - A 1-degree Global Model of Earth's Crust. *Geophys. Res. Abstr.* 15, *Ab-*
686 *str. EGU2013-2658*, 15, Abstract EGU2013–2658. Retrieved from [https://](https://igppweb.ucsd.edu/~gabi/crust1.html)
687 igppweb.ucsd.edu/~gabi/crust1.html
- 688 Lay, T., Duputel, Z., Ye, L., & Kanamori, H. (2013). The December 7, 2012 Japan
689 Trench intraplate doublet (Mw 7.2, 7.1) and interactions between near-trench
690 intraplate thrust and normal faulting. *Phys. Earth Planet. Inter.*, 220, 73–78.
691 doi:10.1016/j.pepi.2013.04.009
- 692 Lay, T., Ye, L., Wu, Z., & Kanamori, H. (2020). Macrofracturing of Oceanic Litho-
693 sphere in Complex Large Earthquake Sequences. *J. Geophys. Res. Solid Earth*,
694 125(10), 1–21. doi:10.1029/2020JB020137
- 695 Lewis, K. B., Collot, J. Y., & Lallemand, S. E. (1998). The dammed Hikurangi
696 Trough: A channel-fed trench blocked by subducting seamounts and their
697 wake avalanches (New Zealand-France GeodyNZ Project). *Basin Res.*, 10(4),

- 698 441–468. doi:10.1046/j.1365-2117.1998.00080.x
- 699 Lewis, K. B., Lallemand, S. E., & Carter, L. (2004). Collapse in a quaternary
700 shelf basin off East Cape, New Zealand: Evidence for passage of a subducted
701 seamount inboard of the ruatoria giant avalanche. *New Zeal. J. Geol. Geophys.*,
702 47(3), 415–429. doi:10.1080/00288306.2004.9515067
- 703 Lomax, A., Michelini, A., & Curtis, A. (2009). Earthquake Location, Direct, Global-
704 Search Methods BT - Encyclopedia of Complexity and Systems Science. *Encycl.*
705 *Complex. Syst. Sci.*, 2449–2473. doi:10.1007/978-0-387-30440-3_150
- 706 Lomax, A., Virieux, J., Volant, P., & Berge-Thierry, C. (2000). Probabilistic Earth-
707 quake Location in 3D and Layered Models BT - Advances in Seismic Event
708 Location. In C. H. Thurber & N. Rabinowitz (Eds.), (pp. 101–134). Dordrecht:
709 Springer Netherlands. doi:10.1007/978-94-015-9536-0_5
- 710 Mason, W. G., Moresi, L., Betts, P. G., & Miller, M. S. (2010). Three-dimensional
711 numerical models of the influence of a buoyant oceanic plateau on subduction
712 zones. *Tectonophysics*, 483(1-2), 71–79. doi:10.1016/j.tecto.2009.08.021
- 713 McGinty, P., Reyners, M., & Robinson, R. (2000). Stress directions in the shal-
714 low part of the Hikurangi subduction zone, New Zealand, from the in-
715 version of earthquake first motions. *Geophys. J. Int.*, 142(2), 339–350.
716 doi:10.1046/j.1365-246X.2000.00155.x
- 717 Meng, L., Ampuero, J. P., Stock, J., Duputel, Z., Luo, Y., & Tsai, V. C. (2012).
718 Earthquake in a maze: Compressional rupture branching during the
719 2012 Mw 8.6 Sumatra earthquake. *Science*, 337(6095), 724–726.
720 doi:10.1126/science.1224030
- 721 Minson, S. E., Simons, M., & Beck, J. L. (2013). Bayesian inversion for finite fault
722 earthquake source models I-theory and algorithm. *Geophys. J. Int.*, 194(3),
723 1701–1726. doi:10.1093/gji/ggt180
- 724 Mitchell, J. S., Mackay, K. A., Neil, H. L., Mackay, E. J., Pallentin, A., & Notman,
725 P. (2012). Undersea New Zealand, 1: 5,000,000. *NIWA chart, Misc. Ser.*,
726 92. Retrieved from [https://niwa.co.nz/our-science/oceans/bathymetry/
727 further-information](https://niwa.co.nz/our-science/oceans/bathymetry/further-information)
- 728 Miyazawa, M., & Mori, J. (2005). Detection of triggered deep low-frequency
729 events from the 2003 Tokachi-oki earthquake. *Geophys. Res. Lett.*, 32(10),
730 1–4. doi:10.1029/2005GL022539
- 731 Mochizuki, K., Henrys, S., Haijima, D., Warren-Smith, E., & Fry, B. (2021). Seismic-
732 ity and velocity structure in the vicinity of repeating slow slip earthquakes,
733 northern Hikurangi subduction zone, New Zealand. *Earth Planet. Sci. Lett.*,
734 563, 116887. Retrieved from <https://doi.org/10.1016/j.epsl.2021.116887>

- 735 doi:10.1016/j.epsl.2021.116887
- 736 Nishikawa, T., & Ide, S. (2014). Earthquake size distribution in subduction zones
737 linked to slab buoyancy. *Nat. Geosci.*, 7(12), 904–908. doi:10.1038/ngeo2279
- 738 Ohta, Y., Miura, S., Ohzono, M., Kita, S., Linuma, T., Demachi, T., . . . Umino, N.
739 (2011). Large intraslab earthquake (2011 April 7, M 7.1) after the 2011
740 off the Pacific coast of Tohoku Earthquake (M 9.0): Coseismic fault model
741 based on the dense GPS network data. *Earth, Planets Sp.*, 63(12), 1207–1211.
742 doi:10.5047/eps.2011.07.016
- 743 Okada, T., & Hasegawa, A. (2003). The M7.1 May 26, 2003 off-shore Miyagi
744 Prefecture Earthquake in northeast Japan: Source process and aftershock
745 distribution of an intra-slab event. *Earth, Planets Sp.*, 55(12), 731–739.
746 doi:10.1186/BF03352482
- 747 Okuwaki, R., Hirano, S., Yagi, Y., & Shimizu, K. (2020). Inchworm-like source
748 evolution through a geometrically complex fault fueled persistent supershear
749 rupture during the 2018 Palu Indonesia earthquake. *Earth Planet. Sci. Lett.*,
750 547, 116449. doi:10.1016/j.epsl.2020.116449
- 751 Okuwaki, R., Yagi, Y., Aránguiz, R., González, J., & González, G. (2016). Rupture
752 Process During the 2015 Illapel, Chile Earthquake: Zigzag-Along-Dip Rupture
753 Episodes. *Pure Appl. Geophys.*, 173(4), 1011–1020. doi:10.1007/s00024-016-
754 1271-6
- 755 Page, M. T., van Der Elst, N., Hardebeck, J., Felzer, K., & Michael, A. J. (2016).
756 Three ingredients for improved global aftershock forecasts: Tectonic region,
757 time-dependent catalog incompleteness, and intersequence variability. *Bull.*
758 *Seismol. Soc. Am.*, 106(5), 2290–2301. doi:10.1785/0120160073
- 759 Petersen, T., Gledhill, K., Chadwick, M., Gale, N. H., & Ristau, J. (2011). The New
760 Zealand National Seismograph Network. *Seismol. Res. Lett.*, 82(1), 9–20.
761 doi:10.1785/gssrl.82.1.9
- 762 Ragon, T., Sladen, A., & Simons, M. (2018). Accounting for uncertain fault geome-
763 try in earthquake source inversions – I: theory and simplified application. *Geo-*
764 *phys. J. Int.*, 214(2), 1174–1190. Retrieved from [https://doi.org/10.1093/gji/](https://doi.org/10.1093/gji/ggy187)
765 [ggy187](https://doi.org/10.1093/gji/ggy187) doi:10.1093/gji/ggy187
- 766 Ranero, C. R., Villaseñor, A., Morgan, J. P., & Weinrebe, W. (2005). Relationship be-
767 tween bend-faulting at trenches and intermediate-depth seismicity. *Geochem-*
768 *istry, Geophys. Geosystems*, 6(12). doi:10.1029/2005GC000997
- 769 Reyners, M., Eberhart-Phillips, D., Stuart, G., & Nishimura, Y. (2006). Imaging
770 subduction from the trench to 300 km depth beneath the central North Is-
771 land, New Zealand, with Vp and Vp/Vs. *Geophys. J. Int.*, 165(2), 565–583.

- 772 doi:10.1111/j.1365-246X.2006.02897.x
- 773 Reyners, M., & McGinty, P. (1999). Shallow subduction tectonics in the Raukumara
774 Peninsula, New Zealand, as illuminated by earthquake focal mechanisms. *J.*
775 *Geophys. Res. Solid Earth*, 104(B2), 3025–3034. doi:10.1029/1998JB900081
- 776 Romeo, I., & Álvarez-Gómez, J. A. (2018). Lithospheric folding by flexural slip in
777 subduction zones as source for reverse fault intraslab earthquakes. *Sci. Rep.*,
778 8(1), 1–9. doi:10.1038/s41598-018-19682-7
- 779 Sandiford, D., Moresi, L., Sandiford, M., & Yang, T. (2019). Geometric
780 controls on flat slab seismicity. *Earth Planet. Sci. Lett.*, 527, 115787.
781 doi:10.1016/j.epsl.2019.115787
- 782 Sandiford, D., Moresi, L. M., Sandiford, M., Farrington, R., & Yang, T. (2020).
783 The Fingerprints of Flexure in Slab Seismicity. *Tectonics*, 39(8).
784 doi:10.1029/2019TC005894
- 785 Scripps Institution Of Oceanography. (1986). *IRIS/IDA Seismic Network*. Interna-
786 tional Federation of Digital Seismograph Networks. doi:10.7914/SN/II
- 787 Shimizu, K., Yagi, Y., Okuwaki, R., & Fukahata, Y. (2020). Development of an inver-
788 sion method to extract information on fault geometry from teleseismic data.
789 *Geophys. J. Int.*, 220(2), 1055–1065. doi:10.1093/gji/ggz496
- 790 Shimizu, K., Yagi, Y., Okuwaki, R., & Fukahata, Y. (2021). Construction of fault
791 geometry by finite-fault inversion of teleseismic data. *Geophys. J. Int.*, 224(2),
792 1003–1014. doi:10.1093/gji/ggaa501
- 793 Simons, M., Fialko, Y., & Rivera, L. (2002). Coseismic deformation from the
794 1999 Mw 7.1 Hector Mine, California, earthquake as inferred from In-
795 SAR and GPS observations. *Bull. Seismol. Soc. Am.*, 92(4), 1390–1402.
796 doi:10.1785/0120000933
- 797 Sippl, C., Schurr, B., Asch, G., & Kummerow, J. (2018). Seismicity Struc-
798 ture of the Northern Chile Forearc From >100,000 Double-Difference
799 Relocated Hypocenters. *J. Geophys. Res. Solid Earth*, 123(5), 4063–4087.
800 doi:10.1002/2017JB015384
- 801 Sleep, N. H., & Ma, S. (2008). Production of brief extreme ground acceleration
802 pulses by nonlinear mechanisms in the shallow subsurface. *Geochemistry, Geo-*
803 *phys. Geosystems*, 9(3), Q03008. doi:10.1029/2007GC001863
- 804 Sokos, E. N., & Zahradnik, J. (2008). ISOLA a Fortran code and a Matlab GUI to per-
805 form multiple-point source inversion of seismic data. *Comput. Geosci.*, 34(8),
806 967–977. doi:10.1016/j.cageo.2007.07.005
- 807 Tadapansawut, T., Okuwaki, R., Yagi, Y., & Yamashita, S. (2021). Rupture Process of
808 the 2020 Caribbean Earthquake Along the Oriente Transform Fault, Involving

- 809 Supershear Rupture and Geometric Complexity of Fault. *Geophys. Res. Lett.*,
810 48(1), 1–9. doi:10.1029/2020GL090899
- 811 Tanioka, Y., Ruff, L., & Satake, K. (1995). The great Kurile Earthquake of
812 October 4, 1994 tore the slab. *Geophys. Res. Lett.*, 22(13), 1661–1664.
813 doi:10.1029/95GL01656
- 814 The Pyrocko Developers. (2017). *Pyrocko: A Versatile Seismology Toolkit for Python*.
815 Retrieved from <http://pyrocko.org> doi:10.5880/GFZ.2.1.2017.001
- 816 Todd, E. K., & Lay, T. (2013). The 2011 Northern Kermadec earthquake doublet and
817 subduction zone faulting interactions. *J. Geophys. Res. Solid Earth*, 118(1), 249–
818 261. doi:10.1029/2012JB009711
- 819 Universidad de Chile Dept de Geofisica (DGF UChile Chile). (1991). *Chilean Na-*
820 *tional Seismic Network*. Retrieved from [https://www.fdsn.org/networks/](https://www.fdsn.org/networks/detail/C/)
821 detail/C/
- 822 University of Tokyo Earthquake Research Institute (Todai ERI Japan). (1989). *Pa-*
823 *cific21 (ERI/STA)*. Retrieved from [https://www.fdsn.org/networks/detail/](https://www.fdsn.org/networks/detail/PS/)
824 PS/
- 825 U.S. Geological Survey Earthquake Hazards Program. (2017). *Advanced National*
826 *Seismic System (ANSS) Comprehensive Catalog of Earthquake Events and Prod-*
827 *ucts*. doi:10.5066/F7MS3QZH
- 828 Vallée, M. (2013). Source time function properties indicate a strain drop in-
829 dependent of earthquake depth and magnitude. *Nat. Commun.*, 4, 1–6.
830 doi:10.1038/ncomms3606
- 831 Vallée, M., Charléty, J., Ferreira, A. M., Delouis, B., & Vergoz, J. (2011). SCARDEC:
832 A new technique for the rapid determination of seismic moment magnitude,
833 focal mechanism and source time functions for large earthquakes using body-
834 wave deconvolution. *Geophys. J. Int.*, 184(1), 338–358. doi:10.1111/j.1365-
835 246X.2010.04836.x
- 836 Wallace, L. M., Reyners, M., Cochran, U., Bannister, S., Barnes, P. M., Berryman, K.,
837 ... Power, W. (2009). Characterizing the seismogenic zone of a major plate
838 boundary subduction thrust: Hikurangi Margin, New Zealand. *Geochemistry,*
839 *Geophys. Geosystems*, 10(10). doi:10.1029/2009GC002610
- 840 Wang, K., & Bilek, S. L. (2011). Do subducting seamounts generate or stop large
841 earthquakes? *Geology*, 39(9), 819–822. doi:10.1130/G31856.1
- 842 Wessel, P., & Luis, J. F. (2017). The GMT/MATLAB Toolbox. *Geochemistry, Geophys.*
843 *Geosystems*, 18(2), 811–823. doi:10.1002/2016GC006723
- 844 Wiens, D. A. (2001). Seismological constraints on the mechanism of deep earth-
845 quakes: Temperature dependence of deep earthquake source properties. *Phys.*

- 846 *Earth Planet. Inter.*, 127(1-4), 145–163. doi:10.1016/S0031-9201(01)00225-4
- 847 Williams, C. A., Eberhart-Phillips, D., Bannister, S., Barker, D. H., Henrys, S., Reyn-
848 ers, M., & Sutherland, R. (2013). Revised interface geometry for the hiku-
849 rangi subduction zone, New Zealand. *Seismol. Res. Lett.*, 84(6), 1066–1073.
850 doi:10.1785/0220130035
- 851 Wiseman, K., Banerjee, P., Bürgmann, R., Sieh, K., Dreger, D. S., & Hermawan,
852 I. (2012). Source model of the 2009 Mw 7.6 Padang intraslab earthquake
853 and its effect on the Sunda megathrust. *Geophys. J. Int.*, 190(3), 1710–1722.
854 doi:10.1111/j.1365-246X.2012.05600.x
- 855 Yabuki, T., & Matsu'ura, M. (1992). Geodetic data inversion using a Bayesian
856 information criterion for spatial distribution of fault slip. *Geophys. J. Int.*,
857 109(2), 363–375. Retrieved from [https://onlinelibrary.wiley.com/doi/](https://onlinelibrary.wiley.com/doi/abs/10.1111/j.1365-246X.1992.tb00102.x)
858 [abs/10.1111/j.1365-246X.1992.tb00102.x](https://onlinelibrary.wiley.com/doi/abs/10.1111/j.1365-246X.1992.tb00102.x)[https://academic.oup.com/gji/](https://academic.oup.com/gji/article-lookup/doi/10.1111/j.1365-246X.1992.tb00102.x)
859 [article-lookup/doi/10.1111/j.1365-246X.1992.tb00102.x](https://academic.oup.com/gji/article-lookup/doi/10.1111/j.1365-246X.1992.tb00102.x) doi:10.1111/j.1365-
860 246X.1992.tb00102.x
- 861 Yagi, Y., & Fukahata, Y. (2011). Introduction of uncertainty of Green's function into
862 waveform inversion for seismic source processes. *Geophys. J. Int.*, 186(2), 711–
863 720. doi:10.1111/j.1365-246X.2011.05043.x
- 864 Yamashita, S., Yagi, Y., Okuwaki, R., Shimizu, K., Agata, R., & Fukahata, Y. (2021).
865 Consecutive ruptures on a complex conjugate fault system during the 2018
866 Gulf of Alaska earthquake. *Sci. Rep.*, 11(1), 5979. doi:10.1038/s41598-021-
867 85522-w
- 868 Ye, L., Lay, T., Bai, Y., Cheung, K. F., & Kanamori, H. (2017). The 2017 Mw 8.2
869 Chiapas, Mexico, Earthquake: Energetic Slab Detachment. *Geophys. Res. Lett.*,
870 44(23), 11,824–11,832. doi:10.1002/2017GL076085
- 871 Ye, L., Lay, T., & Kanamori, H. (2012). Intraplate and interplate faulting interactions
872 during the August 31, 2012, Philippine Trench earthquake (Mw 7.6) sequence.
873 *Geophys. Res. Lett.*, 39(24), 1–6. doi:10.1029/2012GL054164
- 874 Ye, L., Lay, T., & Kanamori, H. (2021). The 25 March 2020 Mw 7.5 Paramushir,
875 northern Kuril Islands earthquake and major (Mw \geq 7.0) near-trench intraplate
876 compressional faulting. *Earth Planet. Sci. Lett.*, 556(March 2020), 116728.
877 doi:10.1016/j.epsl.2020.116728
- 878 Yue, H., Lay, T., & Koper, K. D. (2012). En échelon and orthogonal fault ruptures
879 of the 11 April 2012 great intraplate earthquakes. *Nature*, 490(7419), 245–249.
880 doi:10.1038/nature11492

881 **References From the Supporting Information**

- 882 Ampuero, J.-P., & Dahlen, F. A. (2005). Ambiguity of the Moment Tensor. *Bull. Seis-*
 883 *mol. Soc. Am.*, 95(2), 390–400. doi:10.1785/0120040103
- 884 Bassett, D., Sutherland, R., Henrys, S., Stern, T., Scherwath, M., Benson, A., ... Hen-
 885 derson, M. (2010). Three-dimensional velocity structure of the northern
 886 Hikurangi margin, Raukumara, New Zealand: Implications for the growth of
 887 continental crust by subduction erosion and tectonic underplating. *Geochem-*
 888 *istry, Geophys. Geosystems*, 11(10). doi:10.1029/2010GC003137
- 889 Bird, P. (2003). An updated digital model of plate boundaries. *Geochemistry, Geo-*
 890 *phys. Geosystems*, 4(3), 1105. doi:10.1029/2001GC000252
- 891 Bormann, P. (2012). New Manual of Seismological Observatory Practice (NMSOP-2).
 892 *IASPEI, GFZ Ger. Res. Cent. Geosci.*. doi:10.2312/GFZ.NMSOP-2
- 893 Duputel, Z., Rivera, L., Kanamori, H., & Hayes, G. (2012). W phase source inversion
 894 for moderate to large earthquakes (1990-2010). *Geophys. J. Int.*, 189(2), 1125–
 895 1147. doi:10.1111/j.1365-246X.2012.05419.x
- 896 Dziewonski, A. M., Chou, T.-A., & Woodhouse, J. H. (1981). Determination of
 897 earthquake source parameters from waveform data for studies of global
 898 and regional seismicity. *J. Geophys. Res. Solid Earth*, 86(B4), 2825–2852.
 899 doi:10.1029/JB086iB04p02825
- 900 Eberhart-Phillips, D., Bannister, S., Reyners, M., & Henrys, S. (2020). *New Zealand*
 901 *Wide model 2.2 seismic velocity and Qs and Qp models for New Zealand*. Zenodo.
 902 doi:10.5281/zenodo.3779523
- 903 Eberhart-Phillips, D., Reyners, M., Bannister, S., Chadwick, M., & Ellis, S. (2010).
 904 Establishing a versatile 3-D seismic velocity model for New Zealand. *Seismol.*
 905 *Res. Lett.*, 81(6), 992–1000. doi:10.1785/gssrl.81.6.992
- 906 Ekström, G., Nettles, M., & Dziewoński, A. (2012). The global CMT project
 907 2004–2010: Centroid-moment tensors for 13,017 earthquakes. *Phys. Earth*
 908 *Planet. Inter.*, 200-201, 1–9. doi:10.1016/j.pepi.2012.04.002
- 909 GeoNet. (2021). *GeoNet Earthquake Catalog*. Retrieved from [https://www.geonet.org](https://www.geonet.org.nz/data/types/eq_catalogue)
 910 [.nz/data/types/eq_catalogue](https://www.geonet.org.nz/data/types/eq_catalogue)
- 911 GeoNet Moment Tensors. (2021). *GeoNet Moment Tensors*. Retrieved from [https://](https://github.com/GeoNet/data/tree/main/moment-tensor)
 912 github.com/GeoNet/data/tree/main/moment-tensor
- 913 Hayes, G. P. (2018). *Slab2 - A Comprehensive Subduction Zone Geometry Model: U.S.*
 914 *Geological Survey data release*. doi:10.5066/F7PV6JNV
- 915 Hayes, G. P., Moore, G. L., Portner, D. E., Hearne, M., Flamme, H., Furtney, M., &
 916 Smoczyk, G. M. (2018). Slab2, a comprehensive subduction zone geometry
 917 model. *Science*, 362(6410), 58–61. doi:10.1126/science.aat4723

- 918 Heimann, S., Isken, M., Kühn, D., Sudhaus, H., Steinberg, A., Vasyura-Bathke,
 919 H., ... Dahm, T. (2018). *Grond - A probabilistic earthquake source inver-*
 920 *sion framework*. Retrieved from [http://pyrocko.org/grond/docs/current/](http://pyrocko.org/grond/docs/current/doi:10.5880/GFZ.2.1.2018.003)
 921 [doi:10.5880/GFZ.2.1.2018.003](http://pyrocko.org/grond/docs/current/doi:10.5880/GFZ.2.1.2018.003)
- 922 Kennett, B. L., Engdahl, E. R., & Buland, R. (1995). Constraints on seismic ve-
 923 locities in the Earth from traveltimes. *Geophys. J. Int.*, 122(1), 108–124.
 924 [doi:10.1111/j.1365-246X.1995.tb03540.x](http://doi.org/10.1111/j.1365-246X.1995.tb03540.x)
- 925 Kikuchi, M., & Kanamori, H. (1991). Inversion of complex body waves-
 926 III. *Bull. Seism. Soc. Am.*, 81(6), 2335–2350. Retrieved from [https://](https://pubs.geoscienceworld.org/ssa/bssa/article-abstract/81/6/2335/102472/)
 927 pubs.geoscienceworld.org/ssa/bssa/article-abstract/81/6/2335/102472/
 928 [Inversion-of-complex-body-waves-III](https://pubs.geoscienceworld.org/ssa/bssa/article-abstract/81/6/2335/102472/)
- 929 Laske, G., Masters, T. G., Ma, Z., & Pasyanos, M. (2013). Update on CRUST1.0
 930 - A 1-degree Global Model of Earth's Crust. *Geophys. Res. Abstr.* 15, *Ab-*
 931 *str. EGU2013-2658*, 15, Abstract EGU2013–2658. Retrieved from [https://](https://igppweb.ucsd.edu/~gabi/crust1.html)
 932 igppweb.ucsd.edu/~gabi/crust1.html
- 933 Lomax, A., Michelini, A., & Curtis, A. (2009). Earthquake Location, Direct, Global-
 934 Search Methods BT - Encyclopedia of Complexity and Systems Science. *Encycl.*
 935 *Complex. Syst. Sci.*, 2449–2473. [doi:10.1007/978-0-387-30440-3_150](http://doi.org/10.1007/978-0-387-30440-3_150)
- 936 Lomax, A., Virieux, J., Volant, P., & Berge-Thierry, C. (2000). Probabilistic Earth-
 937 quake Location in 3D and Layered Models BT - Advances in Seismic Event
 938 Location. In C. H. Thurber & N. Rabinowitz (Eds.), (pp. 101–134). Dordrecht:
 939 Springer Netherlands. [doi:10.1007/978-94-015-9536-0_5](http://doi.org/10.1007/978-94-015-9536-0_5)
- 940 Okuwaki, R., Hirano, S., Yagi, Y., & Shimizu, K. (2020). Inchworm-like source
 941 evolution through a geometrically complex fault fueled persistent supershear
 942 rupture during the 2018 Palu Indonesia earthquake. *Earth Planet. Sci. Lett.*,
 943 547, 116449. [doi:10.1016/j.epsl.2020.116449](http://doi.org/10.1016/j.epsl.2020.116449)
- 944 Okuwaki, R., Yagi, Y., Aránguiz, R., González, J., & González, G. (2016). Rupture
 945 Process During the 2015 Illapel, Chile Earthquake: Zigzag-Along-Dip Rupture
 946 Episodes. *Pure Appl. Geophys.*, 173(4), 1011–1020. [doi:10.1007/s00024-016-](http://doi.org/10.1007/s00024-016-1271-6)
 947 [1271-6](http://doi.org/10.1007/s00024-016-1271-6)
- 948 Petersen, T., Gledhill, K., Chadwick, M., Gale, N. H., & Ristau, J. (2011). The New
 949 Zealand National Seismograph Network. *Seismol. Res. Lett.*, 82(1), 9–20.
 950 [doi:10.1785/gssrl.82.1.9](http://doi.org/10.1785/gssrl.82.1.9)
- 951 Shimizu, K., Yagi, Y., Okuwaki, R., & Fukahata, Y. (2020). Development of an inver-
 952 sion method to extract information on fault geometry from teleseismic data.
 953 *Geophys. J. Int.*, 220(2), 1055–1065. [doi:10.1093/gji/ggz496](http://doi.org/10.1093/gji/ggz496)
- 954 Shimizu, K., Yagi, Y., Okuwaki, R., & Fukahata, Y. (2021). Construction of fault

- 955 geometry by finite-fault inversion of teleseismic data. *Geophys. J. Int.*, 224(2),
956 1003–1014. doi:10.1093/gji/ggaa501
- 957 Sokos, E. N., & Zahradnik, J. (2008). ISOLA a Fortran code and a Matlab GUI to per-
958 form multiple-point source inversion of seismic data. *Comput. Geosci.*, 34(8),
959 967–977. doi:10.1016/j.cageo.2007.07.005
- 960 Tadapansawut, T., Okuwaki, R., Yagi, Y., & Yamashita, S. (2021). Rupture Process of
961 the 2020 Caribbean Earthquake Along the Oriente Transform Fault, Involving
962 Supershear Rupture and Geometric Complexity of Fault. *Geophys. Res. Lett.*,
963 48(1), 1–9. doi:10.1029/2020GL090899
- 964 U.S. Geological Survey Earthquake Hazards Program. (2017). *Advanced National*
965 *Seismic System (ANSS) Comprehensive Catalog of Earthquake Events and Prod-*
966 *ucts*. doi:10.5066/F7MS3QZH
- 967 Vallée, M. (2013). Source time function properties indicate a strain drop in-
968 dependent of earthquake depth and magnitude. *Nat. Commun.*, 4, 1–6.
969 doi:10.1038/ncomms3606
- 970 Vallée, M., Charléty, J., Ferreira, A. M., Delouis, B., & Vergoz, J. (2011). SCARDEC:
971 A new technique for the rapid determination of seismic moment magnitude,
972 focal mechanism and source time functions for large earthquakes using body-
973 wave deconvolution. *Geophys. J. Int.*, 184(1), 338–358. doi:10.1111/j.1365-
974 246X.2010.04836.x
- 975 Yagi, Y., & Fukahata, Y. (2011). Introduction of uncertainty of Green's function into
976 waveform inversion for seismic source processes. *Geophys. J. Int.*, 186(2), 711–
977 720. doi:10.1111/j.1365-246X.2011.05043.x
- 978 Yamashita, S., Yagi, Y., Okuwaki, R., Shimizu, K., Agata, R., & Fukahata, Y. (2021).
979 Consecutive ruptures on a complex conjugate fault system during the 2018
980 Gulf of Alaska earthquake. *Sci. Rep.*, 11(1), 5979. doi:10.1038/s41598-021-
981 85522-w
- 982 Ye, L., Lay, T., Bai, Y., Cheung, K. F., & Kanamori, H. (2017). The 2017 Mw 8.2
983 Chiapas, Mexico, Earthquake: Energetic Slab Detachment. *Geophys. Res. Lett.*,
984 44(23), 11,824–11,832. doi:10.1002/2017GL076085